



Title	SPH simulations of binary droplet deformation considering the Fowkes theory
Author(s)	Natsui, Shungo; Tonya, Kazui; Nogami, Hiroshi; Kikuchi, Tatsuya; Suzuki, Ryosuke O.
Citation	Chemical Engineering Science, 229, 116035 https://doi.org/10.1016/j.ces.2020.116035
Issue Date	2021-01-16
Doc URL	http://hdl.handle.net/2115/86549
Rights	© [2021]. This manuscript version is made available under the CC-BY-NC-ND 4.0 license http://creativecommons.org/licenses/by-nc-nd/4.0/
Rights(URL)	http://creativecommons.org/licenses/by-nc-nd/4.0/
Type	article
File Information	CES-D-20-00775R1.pdf



[Instructions for use](#)

14 Abstract:

15 To analyze the complex droplet transient deformation involving two
16 immiscible phases, a practical multi-interfacial tension model has been introduced in the
17 SPH framework. The attraction, which operates on the interface between the different
18 phases is explicitly defined as London dispersion force using the Fowkes theoretical
19 model, and the interfacial tension can be calculated using the sum of the attraction
20 magnitudes corresponding to the surrounding particles. The analytical solution
21 demonstrated good agreement with the simulated results corresponding to the
22 macroscopic multicontact angles and nature of interphase interfacial forces. This simple
23 model is widely applicable to the dynamic analysis of capillary forces involving two or
24 more liquids, and we demonstrated its application to the simulation of the deformation
25 behavior of a binary droplet that contacts a solid. The solid-liquid-liquid contact angle is
26 not sufficient to predict the equilibrium morphology, and the momentum exchange
27 between the two liquids should be considered.

28

29 Keywords: SPH; binary droplet; interfacial tension; Fowkes hypothesis;

30

31 **1. Introduction**

32 The interfacial morphology of two immiscible liquids on a solid surface in a
33 gaseous environment plays an essential role in many industrial processes such as spray
34 combustion in liquid-fuel engines, various food-processing mixing operations, and the
35 processing of petroleum in the context of dispersed water droplets in crude oil. In
36 particular, in pyrometallurgical processes, the interfacial flow of high-temperature
37 liquid-metal-based phase-molten oxides (slag) on the solid materials must be strictly
38 controlled to enhance the smelting efficiency; the base metals in such processes include
39 iron, copper, aluminum, tin, and lead.

40 In the copper smelting process, various forms of molten copper sulfide (matte)
41 - molten slag – solid magnetite as the dispersed phase have been observed, and it is
42 expected that the reaction between several pairs of liquids is dominated by the
43 interphase boundary area (Kemori et al, 1989; Fernández-Caliani et al., 2012;
44 Pérez-Tello et al., 2018). In addition, some noble metals (such as gold and platinum) are
45 also concentrated in the matte, and their loss has a potentially significant economic
46 impact. Although matte and slag are passing at the bottom of the flash smelting furnace,
47 matte droplets containing noble metals remain in the slag phase in the case of
48 insufficient separation, leading to the noble metals in the slag phase being discarded.

49 Despite its notable economic importance, the transient behavior of the interfacial
50 boundary between the matte and slag has yet to be extensively investigated because
51 direct observation of the dynamic behavior of a molten matte–slag boundary is difficult
52 owing to the presence of an extremely limited observation domain (Sauerland et al.,
53 1993; Chung and Cramb, 2000; Fagerlund and Jalkanen, 2000; Han and Holappa, 2003;
54 Bellemans et al., 2017). Conventionally, the morphology of matte–slag liquids has been
55 discussed on the assumption of a core-shell type in which the slag encompasses the
56 matte based on the shape obtained after solidification in equilibrium experiments
57 (Kemori et al, 1989). When droplets of two immiscible liquids immersed in gaseous
58 phase are generally divided to contact three equilibrium topologies, the following three
59 conditions may occur depending on the interfacial tensions balance between the three
60 fluids : (i) The droplets may remain separated (non-engulfing configuration), (ii) one of
61 the phases may completely cover the other one (complete engulfing, which corresponds
62 to the core-shell structure), or (iii) a doublet of droplets may form (partial engulfing)
63 (Torza and Mason, 1970; Pannacci, 2008; Guzowski, 2012). Although this model has
64 succeeded in simplifying the interfacial morphology representation, it is a limited ideal
65 system, and the momentum exchange between two liquids having different physical
66 properties must be considered. The interphase dynamics that involves material

67 discontinuity and force coupling across the interface between different phases has been
68 commonly observed; it, however, represents a challenging topic in terms of numerical
69 modelling and process accounting.

70 Numerical simulations based on the multiphysics model can be used as a
71 powerful tool for predicting the behavior of various melts (Natsui et al, 2017; 2020a;
72 2020b). Several numerical simulations have been carried out to understand the heat and
73 mass transfer phenomena pertaining to dispersed molten sulfide matte–molten oxide
74 slag phases in the commercial furnace (Kemori, et al., 1990; Sasaki et al., 2009).
75 Large-scale simulations, which could be realized owing to the evolution of
76 computational capacity in recent years, are expected to further improve the space
77 resolution and analytical accuracy, and their use would undoubtedly be valuable in the
78 industry. To enable its application to a system with several two-liquids, it is necessary to
79 solve the dynamic form of the droplet with a small calculation load. In recent numerical
80 studies focusing on the collision of immiscible binary droplets, the most common
81 techniques for such calculation include the volume of fluid method (Hoffmann, 2006;
82 Pan and Suga, 2005; Tang, 2016), level set method (Tanguy and Berlemont, 2005), and
83 lattice Boltzmann method (Liang, 2016; Sadullah, 2018; Abadi, 2018). These grid-based
84 Eulerian computational fluid dynamics methods have been used to directly solve the

85 multiphase Navier–Stokes equations. They require computationally expensive interface
86 tracking techniques by introducing an additional field variable defining the position of
87 the interface (Katopodes, 2019). In these methods, explicit tracking of the fluid interface
88 is avoided at the cost of solving an additional hyperbolic equation for the field variable.
89 In these grid-based Eulerian approaches, the main objective is to improve the accuracy
90 of prediction of the evolution of a moving interface. However, these approaches are
91 likely not suitable for the large deformation problem of two or more liquids
92 accompanying severe scattering. Because these models are based on the discretization
93 scheme of space with tetragonal meshes and the interface crosses the interior of the
94 lattice, it is difficult to completely eliminate the numerical diffusion of interfacial shapes
95 across the cell to deal with dispersed phases. Alternatively, as a mesh-free particle
96 method, the smoothed particle hydrodynamics (SPH) method can effectively avoid the
97 abovementioned mesh distortion problem and offer excellent flexibility for simulating
98 the large deformation of liquids (Lucy, 1977; Monaghan, 1988; 1989; 1992; 1994; 2012;
99 Breinlinger, 2013; Yang, 2014). The SPH method is a fully Lagrangian approach that
100 discretizes fluid by moving particles. This approach provides an intuitive description of
101 the fluid flow, because it does not require the consideration of interfacial numerical
102 diffusion even for the dispersed phase. Fortunately, the calculation algorithm (for a

103 weakly compressible viscous flow) can be remarkably simple if a fully explicit time
104 integration procedure is employed.

105 Recently, SPH has been often applied for the description of multiple-fluid flow
106 dynamics by using various improved interfacial representations. Several interfacial
107 tension formulations have been developed to deal with multiphase fluid flow problems,
108 most of which are based on the continuum surface force (CSF) method (Brackbill et al.,
109 1992; Morris, 2000; Hu and Adams, 2006; Rezavand, 2018) or the Cahn–Hilliard model
110 (Cahn and Hilliard, 1958; He et al., 2014). However, this well-known mesh-based
111 interfacial tension model has several issues when applied to a mesh-free particle-based
112 framework, such as the presence of errors in the interfacial curvature calculation and
113 negative pressure contribution, as specified in previous study by Krimi et al. (2018).
114 Although it is necessary to suitably calculate the local interfacial curvature from particle
115 positions, the small number of particles at the interface may limit the computational
116 accuracy in the case of many dispersed droplets being considered under limited
117 computer resources; this problem exists even the number of particles is increased to a
118 satisfactory level, as long as a new interface appears. Furthermore, this approach cannot
119 be easily applied to cases in which the interfacial tension changes locally, such as a
120 Marangoni flow, because the interfacial force component acting tangentially to the

121 surface is ignored in the CSF model (Inagaki, 2018). An alternative formulation of the
122 interfacial tension for the SPH is based on microscopic interphase attractive potentials
123 (Tartakovsky and Meakin, 2005; Kordilla et al., 2013; Li et al., 2018), this approach
124 involves assigning interfacial particles attractive/repulsive forces based on pairwise
125 forces inspired by the molecular origin of the interfacial tension phenomena. Defining
126 these forces to reproduce the effects of interfacial tension led to promising results in
127 several cases involving droplets and flow on a complex solid (Shigorina et al., 2017).
128 Unfortunately, the critical issue of this “potential model” is that the resulting surface
129 tension needs to be calibrated. Although the relationship between interparticle force and
130 interfacial energy has been clarified theoretically (Kondo et al., 2007; Tartakovski and
131 Panchenko, 2016; Nair and Pöschel, 2018), it is not able to be convincingly stated
132 that the verification of calculation and theoretical results has been performed adequately
133 for multiliquid systems. If the interfacial tension between multiple phases can be
134 calculated using a potential model, this technique can be easily applied to a wide range
135 of fields of large-scale systems.

136 To this end, the objectives of the present research are to develop the
137 abovementioned approach for a model that considers multiphase interfacial energy and
138 to verify the computational accuracy of the model based on a comparison of the

139 analytical and theoretical results.

140

141 **2. Numerical methods**

142 **2.1. Basic formulation of SPH**

143 The basic concept of the SPH assumption is the introduction of a kernel
144 function as an integral interpolation to solve a differential equation, such that the fluid
145 dynamics is represented by a set of particle motion equations (Monaghan, 1994); in
146 other words, the formulation is based on an interpolation scheme that allows the
147 estimation of a vector or scalar function f at position \mathbf{r} in terms of the values of the
148 function at the discretization points.

$$f(\mathbf{r}) \cong \int f(\mathbf{r}')W(\mathbf{r} - \mathbf{r}', h)dV, \quad (1)$$

149 where \mathbf{r} and \mathbf{r}' denote arbitrary coordinates, V denotes the volume, and W is the
150 smoothing kernel function with h being the radius of influence. The gradient form of Eq.

151 (1) can be represented as follows:

$$\nabla f(\mathbf{r}) \cong \int \nabla f(\mathbf{r}')W(\mathbf{r} - \mathbf{r}', h)dV. \quad (2)$$

152 This form can be expanded by partial integration as

$$\nabla f(\mathbf{r}) \cong \int \nabla(f(\mathbf{r}')W(\mathbf{r} - \mathbf{r}', h))dV - \int f(\mathbf{r}')\nabla W(\mathbf{r} - \mathbf{r}', h)dV. \quad (3)$$

153 In the general SPH scheme, the first term on the right-hand side can be converted to the

154 boundary integral of the following equation by using the divergence theorem; thus, the
155 kernel function $W(\mathbf{r} - \mathbf{r}', h) = 0$ on the boundary and $\nabla f(\mathbf{r})$ can be expressed as
156 follows:

$$\nabla f(\mathbf{r}) \cong - \int f(\mathbf{r}') \nabla W(\mathbf{r} - \mathbf{r}', h) dV. \quad (4)$$

157 Generally, this is referred to as the final discretization equation in the standard SPH
158 method. Unfortunately, this assumption does not yield in sufficiently accurate solution
159 in the vicinity of the phase boundary. When applying this approximation to dispersed
160 fluids, the discontinuities in the density distribution of the fluids become significant,
161 which leads to an increase in the numerical errors. The moving least squares (MLS)
162 method is widely employed for approximating the function to solve this problem
163 (Colagrossi and Landrini, 2003), which is related to the numerical fluctuations in the
164 pressure at the nearby interface. The pressure is a function of the local density, and thus,
165 the smooth density field of a bulk phase leads to a continuous pressure distribution. The
166 MLS method improves the mass–area–density consistency and filters small-scale
167 pressure oscillations, as described briefly in the subsequent section.

168

169 **2.2. Density approximation**

170 Owing to the compactness, the summation in the function can be replaced with a

171 summation over particles only within the distance h from \mathbf{r}_i ; thus, $W(\mathbf{r}_{ij}, h) = 0$
172 when $|\mathbf{r}_{ij}| > h$. The kernel must possess a symmetrical form to $|\mathbf{r}_{ij}| > 0$. Here, i is the
173 particle index, and j is the index of the neighboring particle around i . The kernel has at
174 least a continuous first derivative and must satisfy the normalization condition,
175 as $\int W(\mathbf{r}_{ij}, h) d\mathbf{r} = 1$. In the $h \rightarrow 0$ limit, the kernel must be reduced to a Dirac delta
176 function $\delta(\mathbf{r}_{ij})$. Wendland's kernel can be applied to avoid various kernel artifacts in a
177 multiphase system (Wendland, 1995; Szewc et al., 2013).

$$W(\mathbf{r}_{ij}, h) = \frac{21}{16\pi h^3} \begin{cases} \left(1 - \frac{q}{2}\right)^4 (2q + 1), & q < 2 \\ 0, & q \geq 2, \end{cases} \quad (5)$$

178 where $|\mathbf{r}_{ij}|_0$ is the interparticle distance corresponding to the initial conditions,
179 $q = |\mathbf{r}_{ij}|/h$, and it was assumed that $h = 1.05|\mathbf{r}_{ij}|_0$ (Natsui et al., 2012; 2014).

180 To express the mass–area–density consistency process, we transformed the SPH
181 formulation into a particle-based format. The density of the particles was expressed in
182 terms of the sum of the kernel functions of the N particles present within the radius of
183 influence, as follows:

$$\rho_i = \sum_{j=1}^N m_j W(\mathbf{r}_{ij}, h), \quad (6)$$

184 where the subscripts i and j denote the particle indices, m is the mass, ρ is the local
185 density around particle, and \mathbf{r}_{ij} is a vector obtained from the difference between the

186 coordinates \mathbf{r}_i and \mathbf{r}_j . Further, m_j is the mass of particle j . Thus, the kernel function
 187 around particle i can be discretized using the following equation, which is derived
 188 from Eqs. (1), (2) and (3).

$$f_i(\mathbf{r}) = \sum_{j=1}^N \frac{m_j}{\rho_j} f(\mathbf{r}_j) W(\mathbf{r}_{ij}, h). \quad (7)$$

189 In this manner, the gradient of f_i can be represented as follows:

$$\nabla f_i(\mathbf{r}) = - \sum_{j=1}^N \frac{m_j}{\rho_j} f(\mathbf{r}_j) \nabla W(\mathbf{r}_{ij}, h). \quad (8)$$

190 SPH is the attractive scheme for simulation of multiphase flows that involve
 191 rapidly changing interfaces between phases, because of its fully Lagrangian formulation.
 192 However, this advantage can be hindered and potentially offset by the possible
 193 occurrence of spurious interface fragmentations. This interface fragmentation artifact is
 194 especially troublesome in flows with high-density/high-viscosity ratio between fluid
 195 phases. In this study, the remedies available in the literature have been introduced in
 196 calculation model. The MLS involves first-order consistent gradient approximation,
 197 which allows the smoothing of pressure, and its first derivative values are obtained
 198 using the abovementioned method in the homogenous bulk phase (Szewc et al., 2013).
 199 The method of the least square interplant with constraint condition (CLS) represents an
 200 improved scheme, which leads to a more accurate approximation around the sampling

201 points than the MLS method does (Natsui et al., 2017; 2018). In the CLS method, by
 202 extending the moving least squares method in the one-dimensional error space for
 203 multiple dimensions, the particles can be made to represent a physical quantity directly.
 204 In the three-dimensional space, the CLS method approximates the values of various
 205 physical parameter around the particles. Refer to a previous report for parameters
 206 determining the procedure (Natsui et al., 2016).

207

208 **2.3. Governing equations of liquid motion and discretization**

209 This section provides the details regarding the SPH scheme for the
 210 discretization of the Navier–Stokes (N–S) equation governing a multiphase flow. The
 211 governing equations for a weakly compressible viscous flow are based on the
 212 relationship between the velocity of sound and the flow density under adiabatic
 213 conditions, as well as the N–S equations:

$$\left(\frac{Dp}{D\rho}\right)_s = c^2, \quad (9)$$

$$\rho \frac{D\mathbf{v}}{Dt} = -\nabla p + \mu \nabla^2 \mathbf{v} + \rho \mathbf{g} + \mathbf{F}_s \quad (10)$$

214 where \mathbf{v} is the fluid velocity, p is the pressure, c is the velocity of sound, μ is the
 215 viscosity, and \mathbf{F}_s is the interfacial force. On the right-hand side of Eq. (10), the first,
 216 second, third, and fourth terms denote the pressure gradient, viscous force, gravity, and

217 interfacial force, respectively. A density function is introduced such that it takes into
 218 account the boundary particles to smoothen each term. Subsequently, the N–S equation
 219 can be formulated considering the simple relationship $\rho = m/V$ as follows:

$$m_i \frac{D\mathbf{v}_i}{Dt} = - \sum_{j=1}^N (\langle p \rangle_i V_i^2 + \langle p \rangle_j V_j^2 + \Pi_{ij}) \nabla W_{ij} \quad (11)$$

$$+ \sum_{j=1}^N \frac{2\mu_i \mu_j}{\mu_i + \mu_j} (V_i^2 + V_j^2) \frac{\mathbf{r}_{ij}}{|\mathbf{r}_{ij}|^2} (\mathbf{v}_i - \mathbf{v}_j) \nabla W_{ij} + m_i \mathbf{g} + \mathbf{F}_s,$$

220 where Π is the artificial viscosity term, which is usually added to the pressure gradient
 221 term to help diffuse sharp variations in the flow and dissipate the energy of the high
 222 frequency term (Monaghan, 1988). The equation for the artificial viscosity is as follows:

$$\Pi_{ij} = \begin{cases} \frac{-\alpha_1 \bar{c}_{ij} \varphi_{ij} + \alpha_2 \varphi_{ij}^2}{\bar{\rho}_{ij}}, & (\mathbf{v}_i - \mathbf{v}_j) \cdot \mathbf{r}_{ij} < 0, \\ 0, & (\mathbf{v}_i - \mathbf{v}_j) \cdot \mathbf{r}_{ij} \geq 0 \end{cases}, \quad (12)$$

$$\varphi_{ij} = \frac{h(\mathbf{v}_i - \mathbf{v}_j) \cdot \mathbf{r}_{ij}}{|\mathbf{r}_{ij}|^2 + (0.1h)^2}, \quad (13)$$

223 where \bar{c}_{ij} and $\bar{\rho}_{ij}$ denote the average values of the sound speed and the density, and
 224 $\alpha_1 = \alpha_2 = 0.01$ are assumed, respectively.

225 To determine the time derivative of pressure, Tait's equation of state can
 226 generally be used (Monagan, 1994).

$$\langle p \rangle_i = \frac{c^2 \rho_0}{\gamma} \left\{ \left(\frac{\rho_i}{\rho_0} \right)^\gamma - 1 \right\}, \quad (14)$$

227 where $\gamma (= 7.0)$ is the adiabatic exponent, ρ_0 is the true density value of the material,

228 and $\langle \cdot \rangle_i$ indicates that the approximated value by using physical model at the position
229 of particle i . Considering the balance of the time step and the volume conservation of
230 the compressible fluid, there must exist an optimal value for c . The sound speed c
231 should be small enough, so that the time step can be increased to an acceptable value for
232 actual calculations. According to Monaghan (1994), c is closely related to the bulk
233 velocity of the flow; that is, $c = \frac{|\mathbf{u}_m|}{Ma}$, where \mathbf{u}_m is the maximum fluid bulk velocity,
234 and Ma is the Mach number. To verify the weak compressibility hypothesis (when
235 $Ma = 0.01$ is assumed), c must be at least 10 times higher than \mathbf{u}_m (Grenier et al.,
236 2013). Therefore, we set $c = 12.24$ m/s.

237

238 **2.4. Interparticle potential force model simply combined with the Fowkes** 239 **hypothesis**

240 In SPH method, it is straightforward to include surface tension models, either
241 using the CSF model or the inter particle interaction force model. It can be said,
242 however, that only the Inter-Particle Force (IPF) model is practical in a system in which
243 three or more interfaces are dispersed. As in the Molecular Dynamics method, the
244 behavior of the fluid–fluid and fluid–fluid–solid interfaces in the IPF-SPH model results
245 from a force balance between pairwise interaction forces. Tartakovsky and Panchenko

246 (2016) developed a pairwise SPH formulation and derived the relationship between the
 247 parameters in IPF and the surface tension and static contact angle. Their approximation
 248 is similar to the SPH approximation of spatial derivatives. Kondo et al. (2007) proposed
 249 simple IPF model based on the definition that surface tension can be considered as the
 250 macro performance of an intermolecular force. Considering the interfacial force \mathbf{F}_s , the
 251 relationship between the interparticle force and interfacial energy has been clarified
 252 theoretically, i.e. the interparticle potential is defined as $E(|\mathbf{r}_{ij}|) = \frac{1}{3}(|\mathbf{r}_{ij}| - \frac{3}{2}|\mathbf{r}_{ij}|_0 +$
 253 $h_s)(|\mathbf{r}_{ij}| - 2h_s)^2$; smoothing length for interfacial tension $h_s = 2.1|\mathbf{r}_{ij}|_0$ (Liu et al.,
 254 2019). The interparticle potential force is defined using the space derivative of $E(|\mathbf{r}_{ij}|)$.
 255 \mathbf{F}_s is localized on the liquid interface by applying it to the liquid elements in the
 256 transition region of the interface; the force per unit volume $\langle \mathbf{F}_s \rangle_i$ is then converted into
 257 a force per unit volume using the relation:

$$\langle \mathbf{F}_s \rangle_i = -2\sigma_i |\mathbf{r}_{ij}|_0^2 \left(\sum_{j=1}^N E(|\mathbf{r}_{ij}|) \right)^{-1} \cdot \sum_{j=1}^N \frac{\partial E(|\mathbf{r}_{ij}|)}{\partial \mathbf{r}} \frac{\mathbf{r}_{ij}}{|\mathbf{r}_{ij}|}, \quad (15)$$

258 where σ_i is the interfacial tension, and E is the interparticle potential. Free surfaces
 259 are generally not smooth, dispersed phase often appeared. In VOF method, it is required
 260 a considerably refined mesh to reproduce all the small-scale droplets normally with
 261 diameter in a wide range, or must ignore them (Li et al., 2016). One of the merits of the
 262 fully-Lagrange method is that it is possible to trace the disperse phase and the

263 continuous phase with the same scheme. Even when $N=1$ in eq. (15), the interfacial
 264 tension can be given by like pairwise force. This model can be simply expanded to
 265 calculate the multiphase interfacial force on the boundary, considering the Fowkes
 266 hypothesis (Fowkes, 1964). The Fowkes hypothesis explains that in a system in which
 267 two immiscible liquids (1 and 2) are in contact, the elements present at the two-phase
 268 interface are subject to forces, as shown in **Fig. 1**. On the interface, liquid 1 receives the
 269 attractive force σ_1 equivalent to the “surface tension” of liquid 1 and the dispersion force
 270 σ_D from liquid 2. The difference between the attractive forces is the force σ_1' acting
 271 on one liquid phase particle at the interface, defined in Eq. (16). The force σ_2' acting
 272 on the interface particles of liquid 2 can be described similarly, as in Eq. (17).

$$\sigma_1' = \sigma_1 - \sigma_D, \quad (16)$$

$$\sigma_2' = \sigma_D - \sigma_2. \quad (17)$$

273 The difference between σ_1' and σ_2' denotes the interfacial tension σ_{12} [Eq. (18)].

$$\sigma_{12} = \sigma_1' - \sigma_2' = \sigma_1 + \sigma_2 - 2\sigma_D \quad (18)$$

274 This simple hypothesis indicates that the unknown dispersion force and interfacial
 275 tension can be calculated explicitly using the surface tension as the input and the
 276 interfacial tension of the two liquids in contact as the conditions.

277 An example of two immiscible droplets contacting on a solid plate is

278 considered, as shown in **Fig. 2**. In terms of the tension balance on the solid–gas–liquid
 279 triple line in which liquid 1, the solid, and gas are in contact, the surface tension σ_1 of
 280 the liquid phase, surface tension σ_3 of the solid phase, and solid–liquid interfacial
 281 tension σ_{31} are considered to be balanced; in other words, Young's equation reflects a
 282 horizontal balance among the interfacial tensions:

$$\sigma_1 \cos \theta_{31} + \sigma_{31} = \sigma_3, \quad (19)$$

283 where θ_{31} is the contact angle between liquid 1 and the solid plate. Here, the unknown
 284 solid surface tension and solid–liquid interfacial tension are eliminated from Young's
 285 equation and Fowkes' equation to obtain the following equation:

$$\cos \theta_{31} = 2 \frac{\sigma_D}{\sigma_1} - 1. \quad (20)$$

286 This equation indicates that the solid–liquid contact angle θ_{31} is determined by the
 287 surface tension of the liquid phase and the dispersion force between the different phases.
 288 The dispersion force is explicitly defined by this equation, and the static contact angle
 289 can be calculated using the interparticle potential model. Furthermore, we similarly
 290 consider other triple lines, that among liquid 2, the solid and gas, and that among the
 291 two liquids and the solid, the Young's equation for which can be written as Eqs. (21) and
 292 (22), respectively.

$$\sigma_2 \cos \theta_{23} + \sigma_{23} = \sigma_3, \quad (21)$$

$$\sigma_{12}\cos\theta_{12} + \sigma_{31} = \sigma_{23} \quad (22)$$

293 Here, θ_{23} is the contact angle between liquid 2 and the solid plate, and θ_{12} is the
 294 contact angle between the two liquids and the solid plate. Eliminating the terms
 295 pertaining to the unknown solid surface tension σ_3 and solid–liquid interfacial tension
 296 σ_{31} and σ_{23} from Eq. (19), (20) and (21), the following equation is obtained.

$$\cos\theta_{12} = \frac{\sigma_1}{\sigma_{12}}\cos\theta_{31} - \frac{\sigma_2}{\sigma_{12}}\cos\theta_{23} \quad (23)$$

297 This indicates that the solid–liquid contact angle θ_{12} is given by the contact angle θ_{31}
 298 and θ_{23} . The variation of θ_{12} with the values of θ_{31} and θ_{23} is shown in **Fig. 3**, which
 299 presents the contact angle mapping for θ_{12} using typical interfacial tension values of
 300 matte and slag. Using this figure, it is possible to predict the wetting behavior when two
 301 immiscible liquids on a solid plate contact each other. When θ_{12} is 0° , liquid 2 mounts
 302 liquid 1 such that it has no contact with the solid phase, and the opposite behavior is
 303 noted when θ_{12} is 180° , with liquid 1 mounting liquid 2. The comparison with the
 304 analytical solution is in the Appendix. All programs are author’s original. Each
 305 computer code was written in Fortran90, and it was compiled and executed by Intel
 306 Fortran composer.

307

308 **3. Analysis of binary droplet deformation**

309 This section describes the SPH simulation for the deformation of two droplets
310 that are initially stationary after they contact under $\mathbf{g} = 0 \text{ m/s}^2$. The simulation was
311 performed to verify the proposed model in the context of the equilibrium morphology
312 based on comparison with the analytical solution. Further, we investigated the
313 oscillation characteristics of a binary droplet.

314

315 **3.1. Two liquids with identical physical properties**

316 *3.1.1. Calculation conditions*

317 **Figure 4** shows the initial placement of two immiscible liquids. The identical
318 physical properties of the liquid phase were assumed to correspond to the molten copper
319 sulfide (matte) phase at 1573 K, as follows: surface tension $\sigma_1 = \sigma_2 = 0.4 \text{ N/m}$,
320 density $\rho_1 = \rho_2 = 4,500 \text{ kg/m}^3$, viscosity $\mu_1 = \mu_2 = 3.13 \times 10^{-3} \text{ Pa}\cdot\text{s}$. Only the
321 interfacial tension between the two liquids, σ_{12} , was varied from 0.2 to 1.0 N/m. A
322 droplet was composed of 19,430 particles, with $|r_{ij}|_0 = 0.06 \text{ mm}$, and the time step
323 $\Delta t = 1.0 \times 10^{-6} \text{ s}$.

324 *3.1.2. Results*

325 **Figure 5** shows the side view of droplet deformation for $\sigma_{12} = 0.2 \text{ N/m}$. All
326 calculations were performed in three dimensions. The two liquids attracted each other

327 due to the interfacial tension, and exhibited an equilibrium shape after oscillation, which
 328 is axially symmetric because of isotropic surface and interfacial tension. **Figure 6**
 329 shows the side view in the equilibrium shape of the binary droplet at each interfacial
 330 tension condition. As σ_{12} increased, the contact area of the two liquids decreased
 331 notably and the distance between the centers of gravity increased. According to the
 332 Fowkes equation, given as Eq. (18), the attractive dispersion force σ_D between the two
 333 phases must decrease with increase in σ_{12} . Under the condition involving fixed σ_1 and
 334 σ_2 ($= 0.4 \text{ N/m}$), the stronger repulsion promotes the separation of the two phases. At
 335 the liquid–liquid–gas triple line, σ_1 , σ_2 and σ_{12} are balanced on the basis of the
 336 Neumann triangle; therefore, a triangle can be considered with sides of lengths σ_1 , σ_2
 337 and σ_{12} . The triangle inequality holds for this triangle, and the following relationship
 338 holds on the triple line.

$$|\sigma_1 - \sigma_2| < \sigma_{12} < \sigma_1 + \sigma_2. \quad (24)$$

339 When $\sigma_2 = \sigma_1$ in this system, Eq. (24) can be written as

$$0 < \sigma_{12} < 2\sigma_1. \quad (25)$$

340 This relation indicates that the liquids separate completely if $\sigma_{12} > 2\sigma_1$. This condition
 341 corresponds to $\sigma_{12} = 1.0 \text{ N/m}$ in Fig. 6, and it can be observed that the proposed
 342 dynamic model predicted this analytical correlation accurately.

343 *3.1.3. Effect of interfacial tension on the oscillation characteristics*

344 Let the centers of gravity of the two liquids be G_1 and G_2 . **Figure 7** shows the
345 time change of the distance between G_1 and G_2 , G_1G_2 , at each value of σ_{12} . Here, G_1G_2
346 was normalized using the initial radius of the droplet. Under all conditions, G_1G_2
347 exhibited damped oscillations. At $t = 0.1$ s, G_1G_2 increased with increase in σ_{12} ,
348 because the interface area between the two liquids decreased, as mentioned above.
349 **Figure 8** shows the oscillation period of the droplets. Here, the oscillation period was
350 defined as the time difference between the minimum and the maximum value of G_1G_2
351 after the droplet oscillated three times. The periods can be noted to be a downward trend
352 when $\sigma_{12} \leq 0.3$ N/m, but they exhibit an increasing tendency at $\sigma_{12} > 0.3$ N/m. This
353 indicates that as σ_{12} increases, the surface tension acting on the free surface in each
354 liquid becomes dominant instead of the attractive force acting on the two-liquid
355 interface. In terms of the oscillation damping, as can be seen in Fig. 7, the two liquids in
356 contact oscillated with decrease in the amplitudes due to viscous force while
357 maintaining a constant oscillation period. Each damping rate of contacting droplets
358 oscillation was shown in **Fig. 9**. Here, the difference between the minimum and
359 maximum values of the curve decreased monotonously with time during the damping,
360 and the rate of decrease was divided by the half period to calculate the damping rate.

361 The lower values of curves indicates that the oscillation damping was weak. Therefore,
362 as σ_{12} increased from 0.1 to 0.3 N/m, the oscillation damping became faster, and at 0.4
363 N/m, the damping rate was the almost same as that at 0.3 N/m despite the fixed
364 viscosities μ_1 and μ_2 . The damping became slower as σ_{12} increased to 0.8 N/m.
365 Under these conditions, the rate of oscillation damping was the highest at $\sigma_{12} =$
366 0.4 N/m.

367 During droplet oscillation, the liquids come in contact to form a two-phase
368 interface; the interface area A increases owing to the liquids attracting each other, and
369 the interfacial energy $F = \sigma_{12} \cdot A$ increases (Natsui et al., 2017; 2020a). Then, the droplets
370 start to move in opposite directions to reduce the excess energy at the equilibrium state,
371 and the interface area decreases. Subsequently, the interface area increases again due to
372 the amount deviated from the energy at equilibrium. After, this deformation is repeated,
373 and an equilibrium shape is obtained via viscous damping. With regard to the oscillation
374 period and viscous damping, a smaller interfacial tension corresponds to a smaller
375 restoring force for the oscillation due to the formation of the interface. Specifically, with
376 a small interfacial tension, the oscillation is dominated by the surface tension acting on
377 the free surface of the droplet, whereas in case a large interfacial tension exists between
378 two liquids, sympathetic oscillation due to the surface tension and interfacial tension

379 becomes apparent. For an interfacial tension of 0.3 N/m or more, the contribution of the
380 interfacial tension to oscillation increases, and the tendency of the two liquids to
381 separate increases; consequently, and the oscillation period is elongated.

382

383 **3.2. Case study for actual matte-slag system**

384 In this section, the interfacial behavior of an actual molten copper sulfide
385 matte–molten slag system is considered. We assumed the physical properties of liquid 1
386 and 2 to correspond to matte and slag, respectively. The physical properties of matte
387 phase was same as section 3.1, for the slag phase, $\sigma_2 = 0.2$ N/m, $\rho_2 = 3,500$ kg/m³,
388 and $\mu_2 = 0.10$ Pa·s. Here, density ratio $\rho_1/\rho_2 = 1.2$, viscosity ratio $\mu_2/\mu_1 = 32$. The
389 initial placement of liquids is the same as that described in section 3.1. The time change
390 of the shape of the liquids is shown in **Fig. 10** ($\sigma_{12} = 0.1$ N/m). In Fig. 10, each vertical
391 cross section was shown to help understanding of the interface shape inside the binary
392 droplet. The asymmetry of the binary droplet is caused by the difference in each surface
393 tension. According to the following well-known Young–Laplace equation, as:

$$\Delta P = \frac{2\sigma}{R}, \quad (26)$$

394 where ΔP represents the pressure difference across the free surface, and R represents
395 the curvature radius of the droplet. Because the surface tension of liquid 1, σ_1 , exceeds

396 σ_2 , the pressure inside liquid 1 becomes larger than that inside liquid 2; consequently,
397 the interfacial morphology between the two phases exhibits a positive curvature on the
398 liquid 2 side, and a lens shape is observed in static state. **Figure 11** shows the
399 determined equilibrium shape at the range of $\sigma_{12} = 0.1$ to 0.6 N/m. In the case of a
400 large σ_{12} , liquids 1 and 2 exhibit a more spherical shape due to a reduction in the
401 attractive force, owing to which the interface area decreases, and G_1G_2 increases. This
402 aspect reflects that a large interfacial tension promotes the separation of the two phases.
403 **Figure 12** shows the schematic diagram of the contact shape of the liquids. In Fig. 12(a),
404 the triple line can be considered at the gas–liquid–liquid contact. At this triple line, the
405 sum of the interfacial forces σ_1 , σ_2 , and σ_{12} must be zero in equilibrium state,
406 according to the Neumann triangle. The tension sum can be calculated using scalar
407 values, by considering a parallel line to rotation axis. Consider the following equation:

$$\sigma_1 \cos \theta_1 - \sigma_2 \cos \theta_2 - \sigma_{12} \cos \theta_{12} = 0, \quad (27)$$

408 where θ represents the angle formed by the tension vector with respect to the rotation
409 axis, as shown in Fig. 12(b). Here, θ_1 and θ_2 can be determined according to the
410 obtained equilibrium shape. The left-hand side of Eq. (27) should ideally be zero;
411 numerical errors, however, are likely to exist. The value on the left-hand side calculated
412 is divided by σ_1 , and the normalized value is defined as an error, the value of which are

413 listed in Table 1. Due to the numerical particle size of the fluid, SPH is not good at thin
414 and wet liquid system. In Table 1, the error increased when σ_{12} was smaller than 0.3
415 N/m due to the small angle formed by σ_2 and σ_{12} as seen in the contact line in Fig. 11.
416 When the interfacial tension is large, the contact line becomes ambiguous since liquid 1
417 has a spherical shape as shown in Fig. 11. In this measurement, since the contact line
418 that was extrapolated from the liquid 2 surface outline was used, the error was thought
419 to have increased due to the way the extrapolated line was made. The average error is
420 approximately 10%, and the particle resolution affects the spatial resolution; this model,
421 however, can express the balance of tension around triple lines.

422 **Figure 13** shows the time change of G_1G_2 under each tension condition. The
423 binary droplet exhibited damped oscillations, and finally reached an equilibrium shape.
424 With increase in σ_{12} , G_1G_2 increased at $t = 0.1$ s. As described in the previous section,
425 as σ_{12} decreased, the interfacial energy of the system, $F = \sigma_{12} \cdot A$, decreased as the
426 interface area decreased, and thus, the two liquids separated and became spherical.
427 **Figure 14** shows the oscillation period of the binary droplet under each interfacial
428 tension. Under the considered conditions, the oscillation period became larger with
429 increase in σ_{12} , likely due to the large interfacial tension that contributed to the
430 separation of the two phases and increase in the amplitude of the oscillation, as

431 described in section 3.1. In addition, the viscosity of liquid 2 was approximately 32
432 times larger than that of liquid 1, which also contributed to the occurrence of rapid
433 oscillation damping. **Figure 15** shows the damping rate of oscillation calculated in the
434 same manner as that shown in Fig. 9. The oscillation damping was more rapid for
435 $\sigma_{12} = 0.1$ to 0.4 N/m and slower for σ_{12} ranging from 0.4 to 0.6 N/m. This
436 tendency is almost similar to that exhibited under the condition of identical physical
437 properties, as described in section 3.1. The oscillation damping of the droplet can be
438 explained by the balance of σ_1 , σ_2 and σ_{12} , even when the density and viscosity of the
439 matte and slag are considered.

440

441 **4. Binary droplet deformation on a flat solid surface**

442 In pyrometallurgical processes, two immiscible liquids often come in contact
443 with the solid surface, and it is important to reveal their morphology and transient
444 behavior in the context of smelting reaction efficiency. In this section, we consider a
445 system in which one spherical liquid droplet with a diameter of 2 mm is placed on a
446 solid plate with a radius of 6 mm under gravity $\mathbf{g} = 9.8$ m/s². The hemispheres of the
447 droplet corresponded to liquids 1 and 2, as shown in **Fig. 16**.

448

449 **4.1. Two liquids with identical physical properties**

450 *4.1.1. Calculation conditions*

451 The identical physical properties of both the liquids were assumed to
452 correspond to the molten copper sulfide matte, as considered in section 3.1. The contact
453 angle between solid and liquid 1, θ_{31} , was set to a constant value of 90° , and only θ_{23}
454 was varied from 30° to 150° .

455 *4.1.2. Results*

456 **Figure 17** shows the time change of the droplet shape on the plate at
457 $\theta_{23} = 60^\circ$ and 120° . Figure 17 (a) and (c) show the cross-sectional views and (b) and
458 (d) show the views from directly overhead for each θ_{23} value. In the case of $\theta_{23} = 60^\circ$,
459 liquid 2 wetted the flat plate under liquid 1 and reached the equilibrium shape. Although
460 the density of both liquids was the same, θ_{23} was smaller than θ_{31} and liquid 2 wet
461 the solid more easily than liquid 1 did. Therefore, liquid 1 rode on liquid 2. The
462 transient shape of the droplet deformed to the lenslike shape observed at equilibrium. At
463 $\theta_{23} = 120^\circ$, liquid 2 found it more difficult to spread on the solid surface than liquid 1
464 did, and thus, liquid 2 rode on liquid 1. **Figure 18** shows the static shape for each value
465 of θ_{23} . Here, the droplet shapes were compared at $t = 0.032$ s. Liquid 1 rode on liquid 2
466 at $\theta_{23} = 30^\circ$ and 60° ; in contrast, liquid 2 rode on liquid 1 at $\theta_{23} = 120^\circ$ and 150° .

467 In the case of $\theta_{23} = 90^\circ$, liquids 1 and 2 were in half contact and the solid–liquid
468 contact angle θ_{12} was 90° . As described in Eq. (23), the solid–liquid contact angle θ_{12}
469 is governed by θ_{31} and θ_{23} . The abovementioned results indicated that the
470 solid–liquid triple line did not exist in the conditions of $\theta_{23} \leq 60^\circ$ or $\theta_{23} \geq 120^\circ$ and
471 corresponded to the diagram of theoretical contact angles shown in Fig. 3 (a).

472

473 **4.2. Case study the actual matte-slag binary droplet on solid surface**

474 To investigate the actual matte–slag–solid system, the density and viscosity of
475 liquid 2 were set as follows: $\rho_2 = 3,500 \text{ kg/m}^3$, and $\mu_2 = 1.00 \times 10^{-1} \text{ Pa}\cdot\text{s}$. The
476 other conditions were the same as in section 4.1. Only θ_{12} was varied from 60° to 120° .
477 **Figure 19** shows the time change of the shape of liquids at each θ_{23} value. Unlike the
478 calculation described in section 4.1, it was empirically noted that the heavier liquid 1
479 pushed out liquid 2 on the slippery solid surface, and they exhibited large relative
480 motion. At $\theta_{23} = 60^\circ$, when both liquids wet the solid plate, liquid 2 wrapped around
481 liquid 1. The entire liquid phase moved slightly to the right of the plate with
482 deformation and reached an equilibrium state. When $\theta_{23} = 90$ and 120° , liquid 2 rode
483 on liquid 1, although liquid 1 remained hemispherical and liquid 1 encompassed liquid
484 2. The entire binary droplet moved to the right of the plate. Because the binary droplet

485 was initially arranged as a hemisphere, the droplet exhibited a sliding motion and
486 deformed from the hemispherical shape to the equilibrium shape. It is considered that
487 the distance of movement on the plate increased as the contact area to the solid phase
488 decreased because a free-slip condition was assumed in this model. The theoretical
489 solid–liquid contact angle θ_{12} under these calculation conditions is shown in the color
490 contour diagram of Fig. 3 (b). According to the findings, the contact triple line of the
491 solid and liquids 1 and 2 is stable only when $\theta_{23} = 90^\circ$, and it does not exist in the
492 equilibrium shape pertaining to $\theta_{23} \leq 60^\circ$ or $\theta_{23} \geq 120^\circ$. Although these are
493 theoretically expected contact states, both the liquids are stably contacted to the solid
494 phase at $\theta_{23} = 60^\circ$. This difference can be explained by the density difference between
495 liquids 1 and 2. When $\rho_1 > \rho_2$, liquid 1 pushes liquid 2 away due to gravity.
496 Simultaneously, liquid 2 partially covers the free surface of liquid 1 because the surface
497 tension of the liquid 2 is smaller than that of the liquid 1 such that the surface–interface
498 energy of the system is reduced. In the case of $\theta_{23} = 90^\circ$, liquid 1 was completely
499 covered by liquid 2, which was also a result of the smaller surface tension of liquid 2.
500 The theoretical value of θ_{12} is 90° in this case; thus, it can be understood that the two
501 liquids are in contact with the solid phase correspondingly. In the case of $\theta_{23} = 120^\circ$,
502 $\theta_{12} = 0^\circ$, and liquid 2 rode on liquid 1. Furthermore, in the system of $\theta_{23} = 90^\circ$, liquid

503 2 rode on liquid 1 and encompassed it.

504 Thus, it was noted that the balance of each interfacial tension, summarized as
505 solid–liquid contact angles, contributed considerably to the change in the form of the
506 two-liquid contact on the solid flat plate. The value of the solid–liquid contact angle was
507 uniquely determined by the physical property of each liquid phase and the solid–liquid
508 contact angle, although its value is not sufficient to predict the equilibrium contact
509 morphology completely, i.e., the momentum due to the density difference between the
510 two liquids should also be considered.

511

512 **5. Conclusion**

513 In this study, we established a model for interfacial tension between multiple
514 phases for a three-dimensional SPH simulation scheme. The interparticle potential
515 based approach was successfully expanded to a multi-interfacial tension model,
516 considering the force balance between multiple phases including the free surface, in
517 terms of the Fowkes theory.

518 We demonstrated the accuracy of the interfacial tension model by examining
519 the equilibrium shape of a binary droplet with a free surface and comparing the results
520 of the simulations with the analytical solutions. The validation was carried out for

521 problems not involving gravity for binary droplet deformation under the
522 surface–interfacial tension force. Satisfactory results that agreed with the theoretical
523 considerations were attained. The oscillation characteristics of binary droplet could be
524 determined via the balance of surface–interfacial tension even when the density and
525 viscosity of the typical molten matte and slag were considered.

526 By further applying this model to a liquid–liquid–solid system including free
527 surfaces, the temporal change in the shape of the binary droplet interface was
528 demonstrated. Consequently, this model could estimate the transient behavior of the
529 interfacial shape by considering the interfacial force balance. The oscillation
530 characteristics of a binary droplet with a free surface were examined and a comparison
531 between the results of the simulations and analytical solutions was performed.
532 Furthermore, the model revealed that the contribution of gravity due to the density
533 difference between the two liquids leads to a more complicated binary droplet
534 morphology.

535 The proposed simplified multiple-fluid dynamic model can be applied in
536 engineering problems because it requires the consideration of simple equations in
537 contrast to the pairwise force model; furthermore, the model exhibits a high accuracy
538 for interfacial shape prediction and has a low computational cost, owing to which it can

539 be used for problems such as those of large-scale dispersed phase flows. The proposed
540 simulation framework can become a valuable tool for future implementations, for fluid
541 flows involving more real phenomena such as the Marangoni effect, heat transfer, and
542 chemical reaction between two liquids, and validations through comparisons between
543 SPH simulations and experimental results.

544

545

Funding

546 This work was made possible by the financial support from the Grant-in-Aid for
547 Scientific Research (KAKENHI grant no. 18K14036, 20H02491) of Japan Society for
548 the Promotion of Science, the Network Joint Research Center for Materials and Devices
549 (no. 20171106), the Iwatani Naoji Foundation (grant no. 16-4323), the Arai Science and
550 Technology Foundation, the Iron and Steel Institute of Japan (ISIJ) Research Promotion
551 Grant, and Steel Foundation for Environmental Protection Technology (SEPT). We
552 would like to thank Editage (www.editage.com) for English language editing.

553

Appendix

554

555 In this section, we verified the computational accuracy of proposed interfacial
556 force model by comparing the numerical results with analytical/experimental results.

557 Theoretical solution exist for the oscillation mode and frequency under zero gravity. The

558 simple and typical form which shows three-dimension has a cube. Lamb's equation is

559 known, where the oscillation period can be calculated by surface tension, droplet radius

560 and liquid density. The vibration mode is axisymmetric oscillation of a droplet with a

561 square cross section, and the equation expresses a period in which the long and short

562 axes are interchanged. Accordingly, the oscillation period is given as $T = \sqrt[3]{\frac{R^3 \cdot \rho}{72\sigma}}$;

563 where R represents the droplet radius, ρ represents the liquid density and σ represents

564 the surface tension of the liquid. In analysis of droplet oscillation by the SPH, it is

565 necessary to clarify the dependency between droplet oscillation and the sound speed c ,

566 as the handling of the quasi-compressibility for spatial discretization using particles and

567 similar factors are considered to influence local motion. Therefore, droplet motion was

568 analyzed for various cases with different sound speed, and compared with analytically

569 estimated oscillation period.

570 The droplet was arranged in a cubic shape with one side of 1 mm initially. The

571 physical properties were as follows: surface tension $\sigma_{\text{sur}}= 0.40$ mN/m , density $\rho=4500$

572 kg/m³, viscosity coefficient $\mu = 3.13 \times 10^{-3}$ Pa·s. As conditions in the numerical
573 calculation, the particle diameter was 0.037 mm, the time step was 2.0×10^{-7} s, and the
574 number of the particles was 19683. In this calculation, the value of c^2 was changed to
575 60, 100, 150, 400, 600 m²/s². Here, Larger c makes higher pressure, and the liquid phase
576 is less likely to be compressed.

577 The droplet deformed by the surface tension over time and reached the
578 equilibrium shape. **Figure A-1** shows the change of the droplet width l over time when
579 $c^2 = 150$ m²/s². The width of the droplet oscillated with damping, and finally l became a
580 constant value. The oscillation period can be calculated by this result. **TABLE A-1**
581 shows the oscillation periods at each value of c^2 . The oscillation period increases as c
582 increases, but c does not greatly affect the oscillation period. This is because the
583 mobility of the liquid particles decreases as the liquid phase tends to be uncompressed.
584 The radius of the equilibrium shaped droplet is 0.6204 mm, and the oscillation period T
585 can be calculated to be 1.21×10^{-3} s with the density 4500 kg/m³ and the surface tension
586 0.40 mN/m. This almost the same as the oscillation period calculated by SPH, especially
587 when $c^2 = 150$ m²/s². Based on this result, the surface tension can be calculated with this
588 numerical model. We selected $c^2 = 150$ m²/s² as the compressibility parameter in the
589 text.

590 For liquid-liquid-solid contact, we observed the contact between water droplet
591 and silicone oil droplet on a Teflon plate, and compared with the equilibrium shape
592 obtained by SPH calculation. A water droplet with a volume of 20 μL was put on the
593 plate, then a silicone oil droplet with 20 μL was put on the water droplet on the plate.
594 The physical properties of water(w) and oil(o) are as follows: the surface tension
595 $\sigma_w=72.8$ mN/m, $\sigma_o=20.1$ mN/m, the water-oil interfacial tension $\sigma_{wo}=52 \times 10^{-3}$ mN/m,
596 the viscosity coefficient $\mu_w=1.5 \times 10^{-3}$ Pa·s, $\mu_o=9.35$ Pa·s, the contact angle to the
597 Teflon surface $\theta_w=108.9$ deg, $\theta_o=16.4$ deg. Figure A-2 shows the water-oil contact
598 morphology on the Teflon plate. As shown in experimental photograph, the oil covered
599 the surface of the water phase which have a larger surface tension. Oil with a small
600 contact angle spreads on the plate, and a water droplet exists in the center. The contact
601 line of oil was affected by the surface state of the plate, and it became an distorted shape
602 without spreading isotropically. An ambiguous outline of water droplet can be observed,
603 but it is difficult to determine the exact outline of the water-oil interface because of the
604 influence of the difference in refractive index between water and oil, and this must be
605 solved in the future. According to the Eq. (23), the contact angle θ_{wo} when the
606 water-oil-Teflon plate contacts can be calculated with the physical properties described
607 above, and θ_{wo} is 145.5 deg. This indicates that there exists a water-oil-plate contact

608 angle, which implies that there is no oil layer between the water droplet and the plate,
609 and the water droplet contacts with the plate directly. For Fig. A-2(a), the oil covered the
610 surface of the water droplet, and outline of the whole droplet is in good agreement with
611 the experiment. The water-oil interface, which was difficult to observe in the actual
612 droplet, was shown in result, and water droplet was in contact with the plate. The water
613 droplet did not spread on the substrate and became spherical. For Fig. A-2(b), the
614 droplet was wet and spreaded isotropically because the surface of the plate was smooth,
615 and the oil contact line became circular. Compared to the experiment, the radius of the
616 contact line circle was smaller, and this depends on particle resolution, and it is
617 considered that oil will spread thinly and widely if the number of the particles is ensured.
618 The calculated contact angle was obtained from the equilibrium shape, and the
619 water-oil-plate contact angle $\theta_A=147.3$ deg and the oil-plate contact angle $\theta_B=24.0$ deg.
620 The given contact angles are 145.4 deg and 16.4 deg respectively, and the
621 water-oil-plate contact angle well agrees with calculated value. For the contact line
622 between the oil and the plate, smaller contact angle made the oil phase thinner.
623 Therefore, it is considered that the size of the particles having a certain radius, and the
624 contact angle was estimated to be larger.

625 As discribed above, the oscillation of a single droplet and the contact of

626 water-oil-plate were calculated, and it was verified that surface and interfacial tension
627 can be calculated with high accuracy in this SPH.

References

628

629 Abadi, R. H. H., Rahimian, M. H., & Fakhari, A., 2018. Conservative phase-field
630 lattice-Boltzmann model for ternary fluids. *J. Comput. Phys.*, **374**, 668-691.

631

632 Bellemans, I., De Wilde, E., Blanpain, B., Moelans, N., & Verbeken, K. 2017.
633 Investigation of Origin of Attached Cu-Ag Droplets to Solid Particles During
634 High-Temperature Slag/Copper/Spinel Interactions. *Metall. Mater. Trans. B*, **48**(6),
635 3058-3073.

636

637 Brackbill, J. U., D. B. Kothe, and C. Zemach, 1992. "A continuum method for modeling
638 surface tension", *J. Comput. Phys.*, **100**, 335-354.

639

640 Breinlinger, T., Polfer, P., Hashibon, A., & Kraft, T. 2013. Surface tension and wetting
641 effects with smoothed particle hydrodynamics. *J. Comput. Phys.*, **243**, 14-27.

642

643 Cahn, J. W., and J. E. Hilliard, 1958. "Free energy of a nonuniform system. I. Interfacial
644 free energy", *J. Chem. Phys.*, **28**(2), 258-267.

645

646 Chung, Y., & Cramb, A. W. (2000). Dynamic and equilibrium interfacial phenomena in
647 liquid steel-slag systems. *Metall. Mater. Trans. B*, **31**(5), 957-971.

648

649 Colagrossi, A., and M. Landrini, 2003. “Numerical simulation of interfacial flows by
650 smoothed particle hydrodynamics”, *J. Comput. Phys.*, **191**, 448–475.

651

652 Fagerlund, K. O., & Jalkanen, H. 2000. Microscale simulation of settler processes in
653 copper matte smelting. *Metall. Mater. Trans. B*, **31**(3), 439-451.

654

655 Fernández-Caliani, J. C., Ríos, G., Martínez, J., & Jiménez, F. 2012. Occurrence and
656 speciation of copper in slags obtained during the pyrometallurgical processing of
657 chalcopyrite concentrates at the Huelva smelter (Spain). *J. Mining and Metall. B:*
658 *Metallurgy*, **48**(2), 161-171.

659

660 Fowkes, F. M. (1964). Attractive Forces at Interfaces, *Ind. Eng. Chem.* **56** (12), 40-52.

661

662 Grenier, N., D. Le Touzé, A. Colagrossi, M. Antuono, and G. Colicchio, 2013. “Viscous
663 bubbly flows simulation with an interface SPH model”, *Ocean Eng.*, **69**, 88–102.

664

665 Guzowski, J., Korczyk, P. M., Jakiela, S., & Garstecki, P., 2012. The structure and
666 stability of multiple micro-droplets. *Soft Matter*, **8**(27), 7269-7278.

667

668 Han, Z., & Holappa, L. 2003. Mechanisms of iron entrainment into slag due to rising
669 gas bubbles. *ISIJ Int.*, **43**(3), 292-297.

670

671 He, X., Wang, H., Zhang, F., Wang, H., Wang, G., & Zhou, K. 2014. Robust simulation
672 of sparsely sampled thin features in SPH-based free surface flows. *ACM Trans. Graph.*
673 *(TOG)*, **34**(1), 1-9.

674

675 Hoffmann, A., Ausner, I., & Wozny, G., 2006. Detailed investigation of multiphase
676 (gas–liquid and gas–liquid–liquid) flow behaviour on inclined plates. *Chem. Eng. Res.*
677 *Design*, **84**(2), 147-154.

678

679 Hu, X. Y., and N.A. Adams, 2006. “A multi-phase SPH method for macroscopic and
680 mesoscopic flows”, *J. Comput. Phys.*, **213**(2), 844-861.

681

682 Inagaki, K., 2018. Improved models of surface tension and air resistance for
683 multiphysics particle method., *J. Nucl. Sci. Technol.*, **55**(2), 169-180.

684

685 Katopodes, N. D., 2019. Free-surface Flow computational methods,
686 Butterworth-Heinemann, 1st ed., Elsevier. (pp. 768-828)

687

688 Kemori, N., Denholm, W. T., & Kurokawa, H. 1989. Reaction mechanism in a copper
689 flash smelting furnace. *Metall Mater. Trans. B*, **20**(3), 327-336.

690

691 Kemori, N., Ojima, Y., & Kondo, Y. 1990. Optical Microscopic Examination of
692 Suspended Copper Concentrate Particles in a Flash Furnace. I. Investigation of the
693 Reactions in a Copper Flash Smelting Shaft. *J. MMIJ*, **106**, 545-550.

694

695 Kondo, M., Koshizuka, S., Suzuki, K., & Takimoto, M. (2007, January). Surface tension
696 model using inter-particle force in particle method. In *ASME/JSME 2007 5th joint fluids
697 engineering conference* (pp. 93-98). American Society of Mechanical Engineers Digital
698 Collection.

699

700 Kordilla, J., Tartakovsky, A. M., & Geyer, T. 2013. A smoothed particle hydrodynamics
701 model for droplet and film flow on smooth and rough fracture surfaces. *Adv. water*
702 *resour.*, **59**, 1-14.

703

704 Krimi, A., Rezoug, M., Khelladi, S., Nogueira, X., Deligant, M., & Ramírez, L. 2018.
705 Smoothed particle hydrodynamics: a consistent model for interfacial multiphase fluid
706 flow simulations. *J. Comput. Phys.*, **358**, 53-87.

707

708 Lancaster, P., and K. Salkauskas, 1981. “Surfaces Generated by Moving Least
709 SquaresMethods”, *Math. Comput.*, **37**, 141-158.

710

711 Li, L., Shen, L., Nguyen, G. D., El-Zein, A., & Maggi, F., 2018. A smoothed particle
712 hydrodynamics framework for modelling multiphase interactions at meso-scale. *Comput.*
713 *Mech.*, **62**(5), 1071-1085.

714

715 Li, M., Li, Q., Kuang, S., & Zou, Z., 2016. Computational investigation of the splashing
716 phenomenon induced by the impingement of multiple supersonic jets onto a molten
717 slag–metal bath. *Industrial & Engineering Chemistry Research*, **55**(12), 3630-3640.

718

719 Liang, H., Shi, B. C., & Chai, Z. H., 2016. Lattice Boltzmann modeling of three-phase
720 incompressible flows. *Phys. Rev. E*, **93**(1), 013308.

721

722 Liu, Q. X., Sun, Z. G., Sun, Y. J., Chen, X., & Xi, G., 2019. Numerical investigation of
723 liquid dispersion by hydrophobic/hydrophilic mesh packing using particle method.
724 *Chemical Engineering Science*, **202**, 447-461.

725

726 Lucy, L. B., 1977. A numerical approach to the testing of the fission
727 hypothesis. *Astronom. J.*, **82**, 1013-1024.

728

729 Monaghan, J. J., 1988. "An introduction to SPH", *Comput. Phys. Commun.*, **48**, 89-96.

730

731 Monaghan, J. J., 1989. "On the Problem of Penetration in Particle Methods", *J. Comput.*
732 *Phys.*, **82**, 1-15.

733

734 Monaghan, J. J., 1992. "Smoothed particle hydrodynamics", *Annu. Rev. Astron.*
735 *Astrophys.*, **30**, 543-574

736

737 Monaghan, J. J., 1994. “Simulating free surface flows with SPH”, *J. Comput. Phys.*, **110**,
738 399–406.

739

740 Monaghan, J. J., 2012. “Smoothed particle hydrodynamics and its diverse applications”,
741 *Ann. Rev. Fluid Mech.*, **44**, 323–346.

742

743 Morris, J. P., 2000. “Simulating surface tension with smoothed particle hydrodynamics”,
744 *Int. J. Num. Meth. Fluids*, **33**, 333–353.

745

746 Nair, P., & Pöschel, T., 2018. Dynamic capillary phenomena using Incompressible
747 SPH. *Chem. Eng. Sci.*, **176**, 192-204.

748

749 Natsui, S., Soda, R., Kon, T., Ueda, S., Kano, J., Inoue R., and Ariyama, T., 2012,
750 Wettability Model Considering Three-phase Interfacial Energetics in Particle Method,
751 *Mater. Trans.*, **53**(4), 662-670.

752

753 Natsui, S., Takai, H., Kumagai, T., Kikuchi, T., & Suzuki, R. O. 2014. Stable mesh-free
754 moving particle semi-implicit method for direct analysis of gas–liquid two-phase
755 flow. *Chemical Engineering Science*, **111**, 286-298.

756

757 Natsui, S., Nashimoto, R., Takai, H., Kumagai, T., Kikuchi, T., & Suzuki, R. O. 2016.
758 SPH simulations of the behavior of the interface between two immiscible liquid stirred
759 by the movement of a gas bubble. *Chem. Eng. Sci.*, **141**, 342-355.

760

761 Natsui, S., Nashimoto, R., Kumagai, T., Kikuchi, T., & Suzuki, R. O. 2017. An SPH
762 Study of Molten Matte–Slag Dispersion. *Metall. Mater. Trans. B*, **48**(3), 1792-1806.

763

764 Natsui, S., Sawada, A., Terui, K., Kashihara, Y., Kikuchi, T., & Suzuki, R. O. 2018.
765 DEM-SPH study of molten slag trickle flow in coke bed. *Chemical Engineering Science*,
766 **175**, 25-39.

767

768 Natsui, S., Tonya, K., Nogami, H., Kikuchi, T., Suzuki, R. O., Ohno, K. Sukenaga, S.,
769 Kon, T., Ishihara S., and Ueda, S., 2020a, Numerical study of binary trickle flow of

770 liquid iron and molten slag in coke bed by smoothed particle hydrodynamics, *Processes*,
771 **8**(2), 221.

772

773 Natsui, S., Ishihara, S., Kon, T., Ohno, K. I., & Nogami, H. 2020b. Detailed modelling
774 of packed-bed gas clogging due to thermal-softening of iron ore by
775 Eulerian–Lagrangian approach. *Chemical Engineering Journal*, **392**, 123643.

776

777 Pan, Y., & Suga, K., 2005. Numerical simulation of binary liquid droplet collision. *Phys.*
778 *Fluids*, **17**(8), 082105.

779

780 Pannacci, N., Bruus, H., Bartolo, D., Etchart, I., Lockhart, T., Hennequin, Y., Willaime,
781 H., & Tabeling, P. 2008. Equilibrium and nonequilibrium states in microfluidic double
782 emulsions. *Phys. Rev. Let.*, **101**(16), 164502.

783

784 Pérez-Tello, M., Parra-Sánchez, V. R., Sánchez-Corrales, V. M., Gómez-Álvarez, A.,
785 Brown-Bojórquez, F., Parra-Figueroa, R. A., E. R. Balladares-Varela &
786 Araneda-Hernández, E. A. 2018. Evolution of size and chemical composition of copper

787 concentrate particles oxidized under simulated flash smelting conditions. *Metall. Mater.*
788 *Trans. B*, **49**(2), 627-643.

789

790 Rezavand, M., Taeibi-Rahni, M., & Rauch, W., 2018. An ISPH scheme for numerical
791 simulation of multiphase flows with complex interfaces and high density ratios. *Comput.*
792 *Mathe. Appl.*, **75**(8), 2658-2677.

793

794 Sadullah, M. S., Semprebon, C., & Kusumaatmaja, H., 2018. Drop dynamics on
795 liquid-infused surfaces: The role of the lubricant ridge. *Langmuir*, **34**(27), 8112-8118.

796

797 Sasaki, Y., Mori, Y., Miura, T., & Aoki, H. 2009. Numerical Study of Combustion
798 Phenomena in Flash Smelting Furnace Considering Collisions of Concentrate
799 Particles. *J. MMIJ*, **125**(3), 129-134.

800

801 Sauerland, S., Lohöfer, G., & Egry, I. 1993. Surface tension measurements on levitated
802 liquid metal drops. *J. non-crystalline solids*, **156**, 833-836.

803

804 Shigorina, E., Kordilla, J., & Tartakovsky, A. M., 2017. Smoothed particle
805 hydrodynamics study of the roughness effect on contact angle and droplet flow. *Phys.*
806 *Rev. E*, **96**(3), 033115.

807

808 Szewc, K., J. Pozorski, and J. P. Minier, 2013. “Simulations of single bubbles rising
809 through viscous liquids using Smoothed Particle Hydrodynamics”, *Int. J. Multiphase*
810 *Flow*, **50**, 98-105.

811

812 Tang, C., Zhao, J., Zhang, P., Law, C. K., & Huang, Z., 2016. Dynamics of internal jets
813 in the merging of two droplets of unequal sizes. *J. Fluid Mech.*, **795**, 671-689.

814

815 Tanguy, S., & Berlemont, A., 2005. Application of a level set method for simulation of
816 droplet collisions. *Int. J. Multiphase Flow*, **31**(9), 1015-1035.

817

818 Tartakovsky, A. and P. Meakin, 2005. “Modeling of surface tension and contact angles
819 with smoothed particle hydrodynamics”, *Phys. Rev. E*, **72**, 026301.

820

821 Tartakovsky, A. M., & Panchenko, A., 2016. Pairwise force smoothed particle
822 hydrodynamics model for multiphase flow: surface tension and contact line dynamics. *J.*
823 *Comput. Phys.*, **305**, 1119-1146.

824

825 Torza, S., & Mason, S. G. 1970. Three-phase interactions in shear and electrical fields. *J.*
826 *colloid Interf. Sci.*, **33**(1), 67-83.

827

828 Wendland, H., 1995, “Piecewise polynomial, positive definite and compactly supported
829 radial functions of minimal degree”, *Adv. Comput. Math.* **4**, 389–396.

830

831 Yang, X., Liu, M., & Peng, S. 2014. Smoothed particle hydrodynamics modeling of
832 viscous liquid drop without tensile instability. *Computers & Fluids*, **92**, 199-208.

833

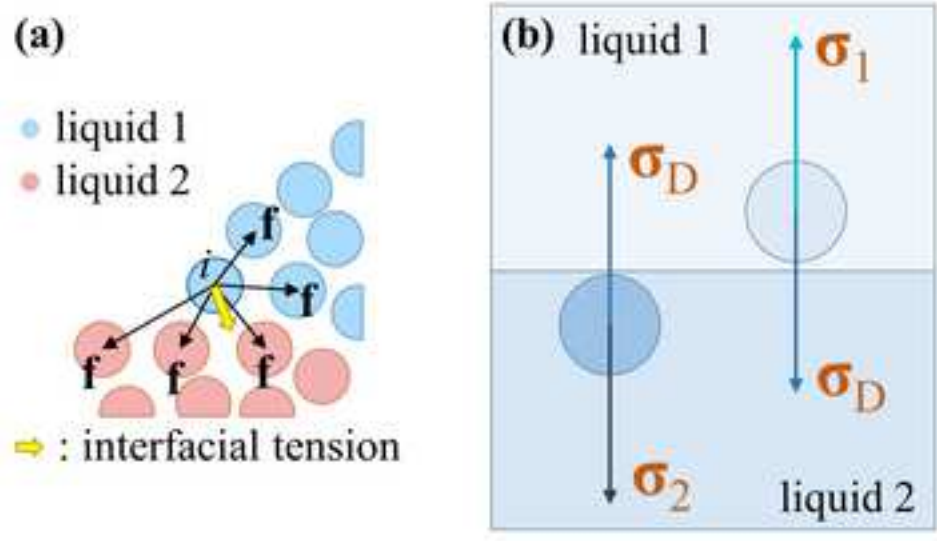


Fig.1 Schematic of interfacial interaction between immiscible liquid phases (a) for interparticle potential model and (b) for Fowkes theory. f in (a) denotes an attractive force.

Figure
[Click here to download high resolution image](#)

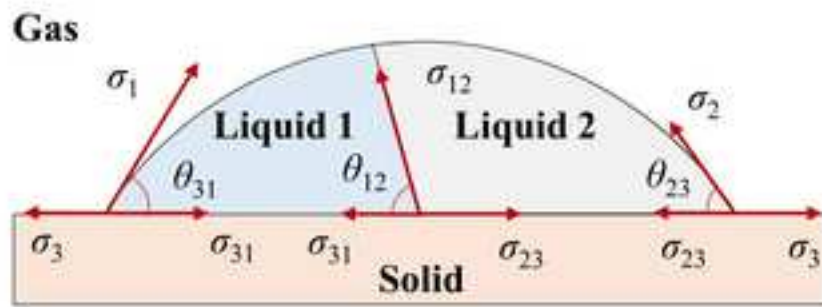


Fig.2 Depicted two contacting liquid droplets on a flat surface and these force balance.

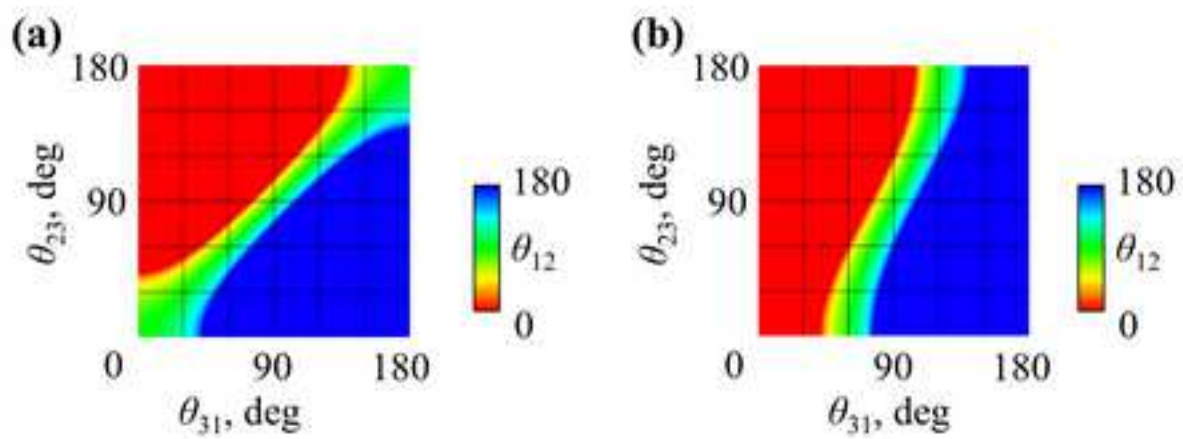
Figure[Click here to download high resolution image](#)

Fig.3 Contact angle value θ_{12} which is calculated by eq. 26. (a: $\sigma_1=0.4$ N/m, $\sigma_2=0.4$ N/m, $\sigma_3=0.1$ N/m, b: $\sigma_1=0.4$ N/m, $\sigma_2=0.2$ N/m, $\sigma_3=0.1$ N/m)

Figure
[Click here to download high resolution image](#)

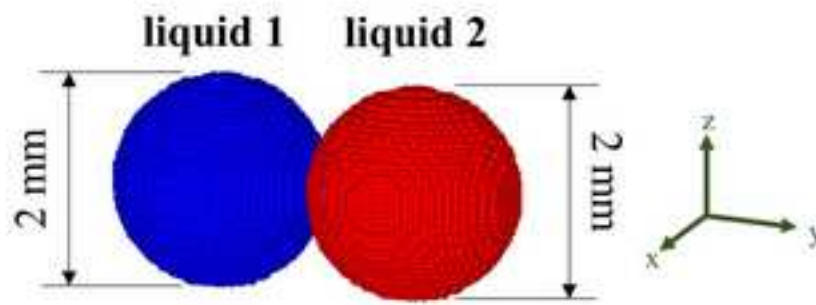


Fig.4 Initial placement of two droplets.

Figure

[Click here to download high resolution image](#)

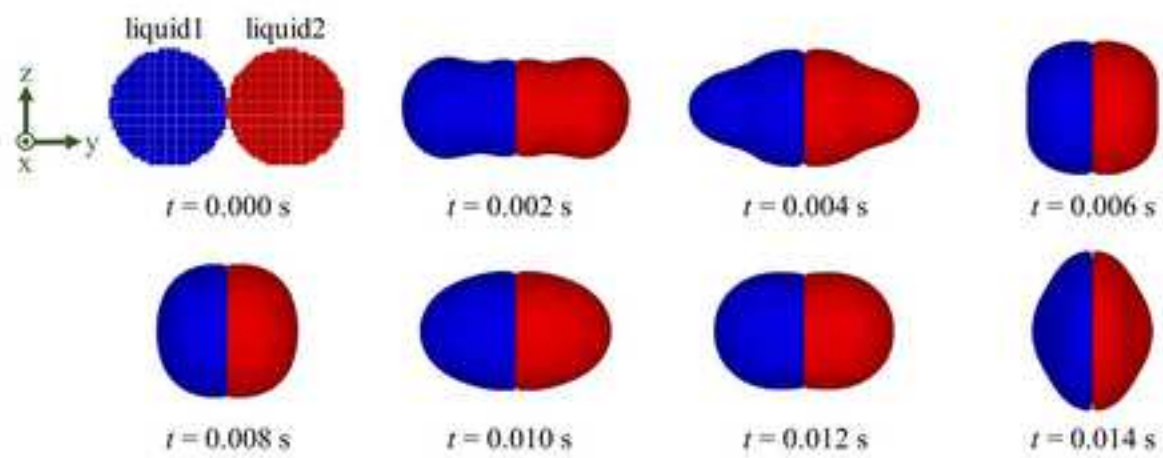


Fig.5 Time change of binary droplet morphologies at $\sigma_{12} = 0.2$ N/m.

Figure
[Click here to download high resolution image](#)

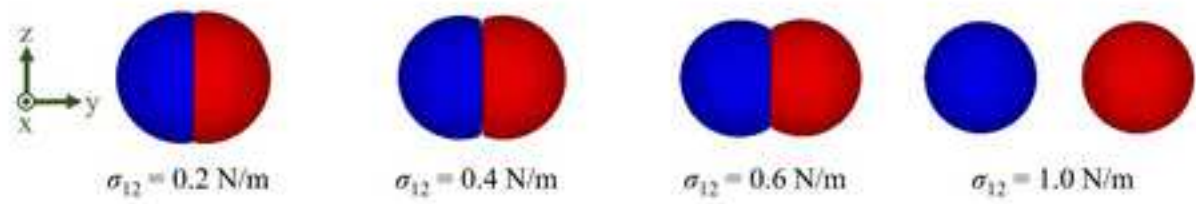


Fig.6 Equilibrium shape of binary droplet at each value of σ_{12} .

Figure

[Click here to download high resolution image](#)

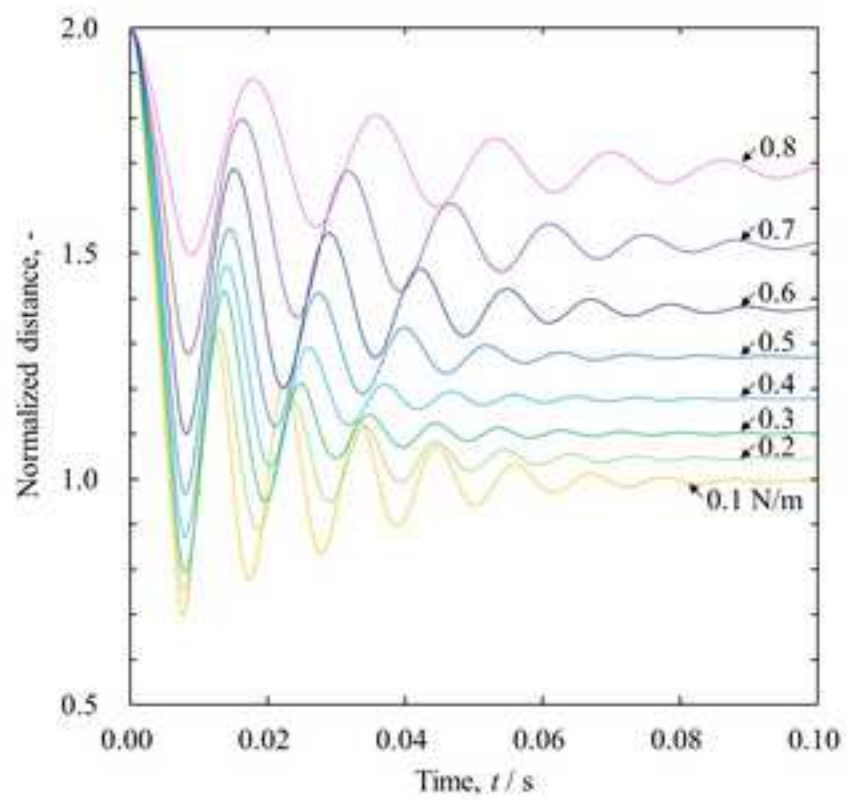


Fig.7 Time change of the normalized G_1G_2 by initial diameter of the droplet in each σ_{32} value.

Figure
[Click here to download high resolution image](#)

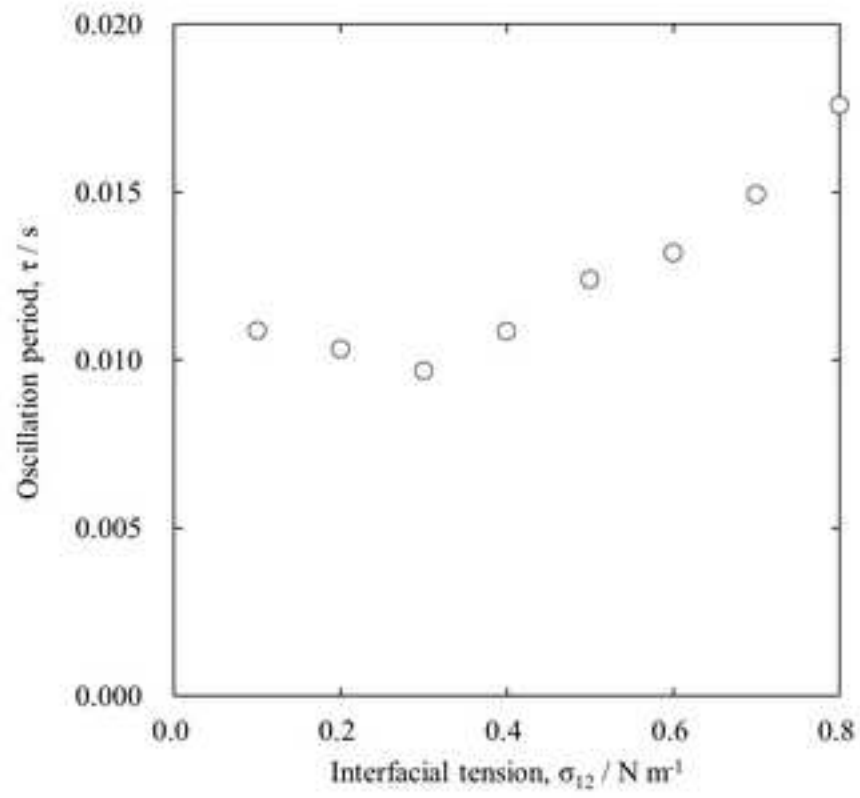


Fig.8 Oscillation periods at each σ_{12} value.

Figure
[Click here to download high resolution image](#)

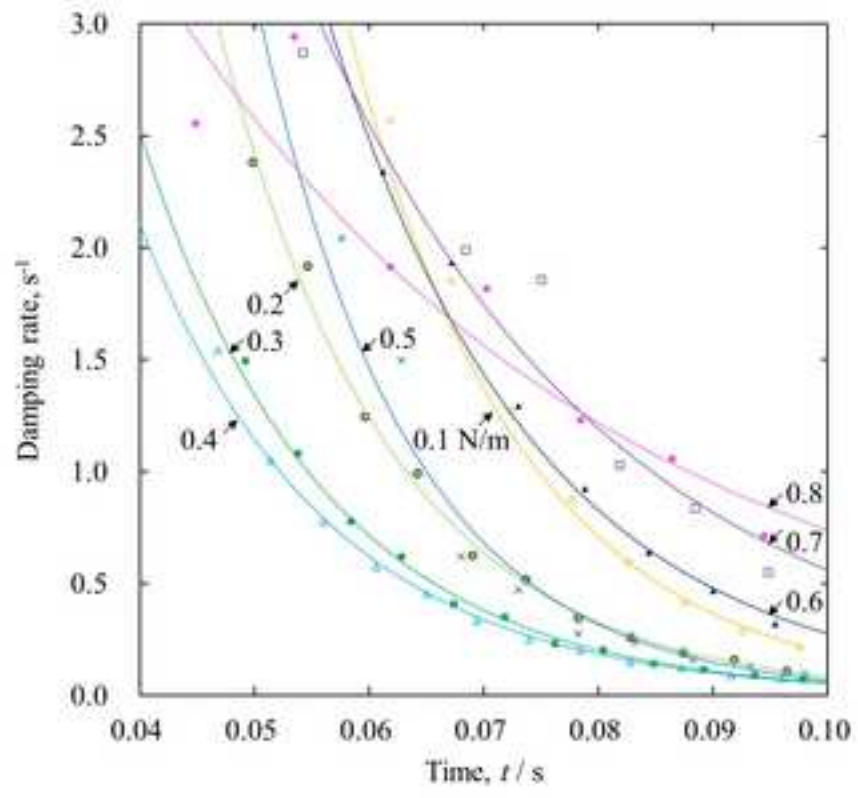


Fig.9 Damping rate of contacting droplets oscillation at each interfacial tension value.

Figure

[Click here to download high resolution image](#)

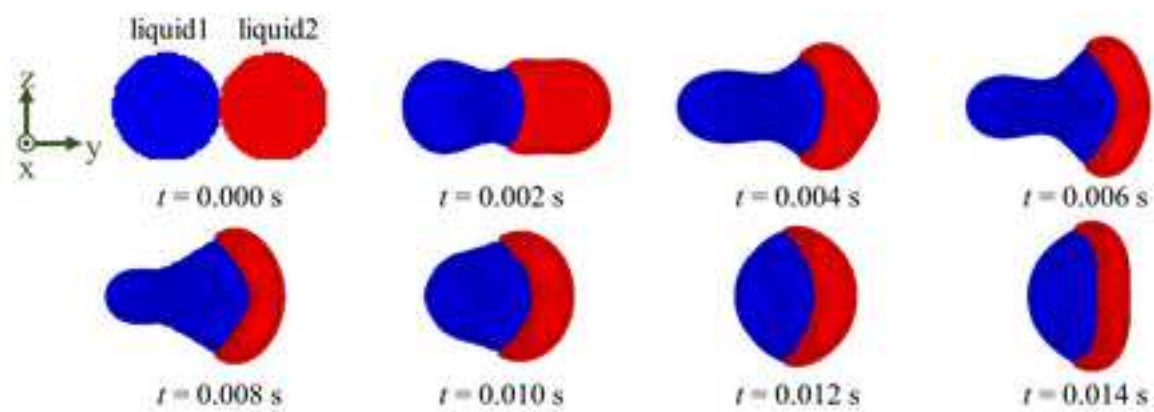


Fig.10 Time change of binary droplet morphologies assumed to be matte and slag at $\sigma_{12} = 0.1$ N/m.

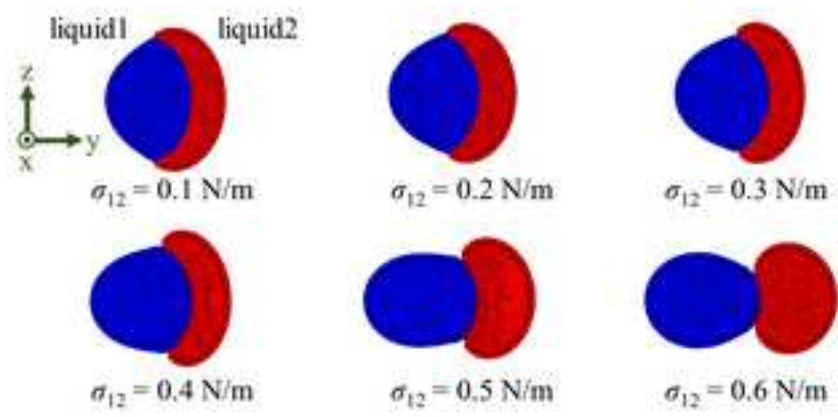


Fig.11 The equilibrium shapes of contacting two droplets at each interfacial tension value.

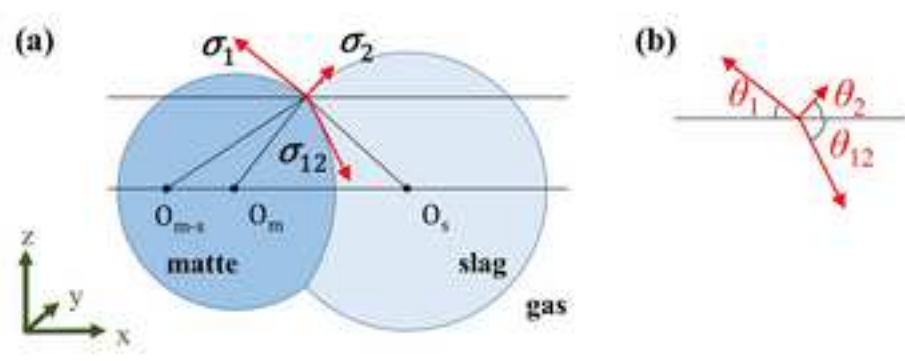


Fig.12 The schematic diagram of contacting two droplets.

Figure

[Click here to download high resolution image](#)

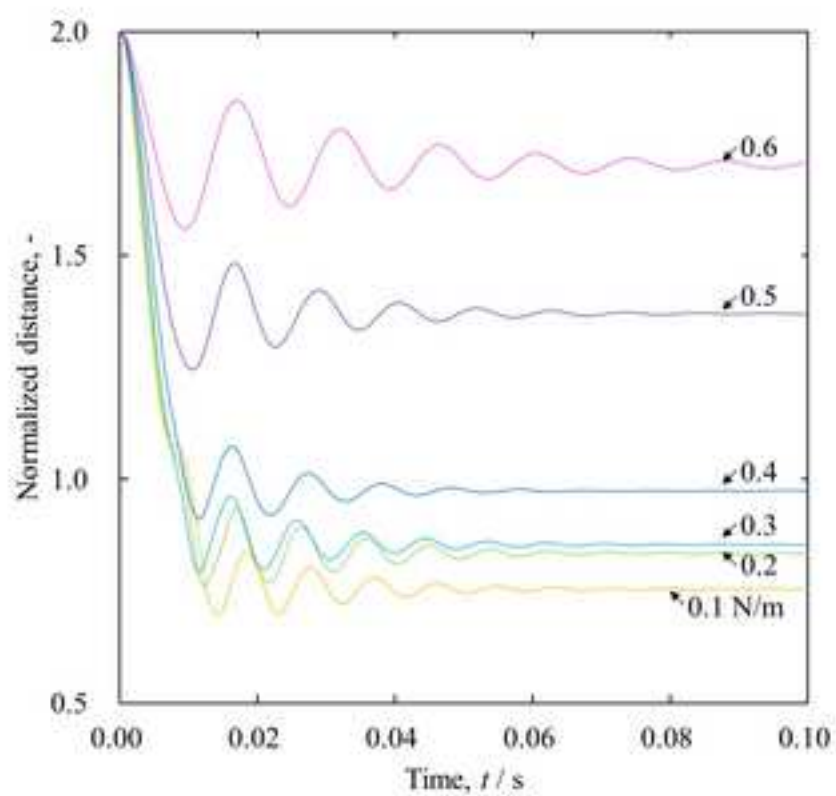


Fig.13 Time change of the normalized G_1G_2 by initial diameter of the droplet assumed to be matte and slag at each σ_{12} value.

Figure
[Click here to download high resolution image](#)

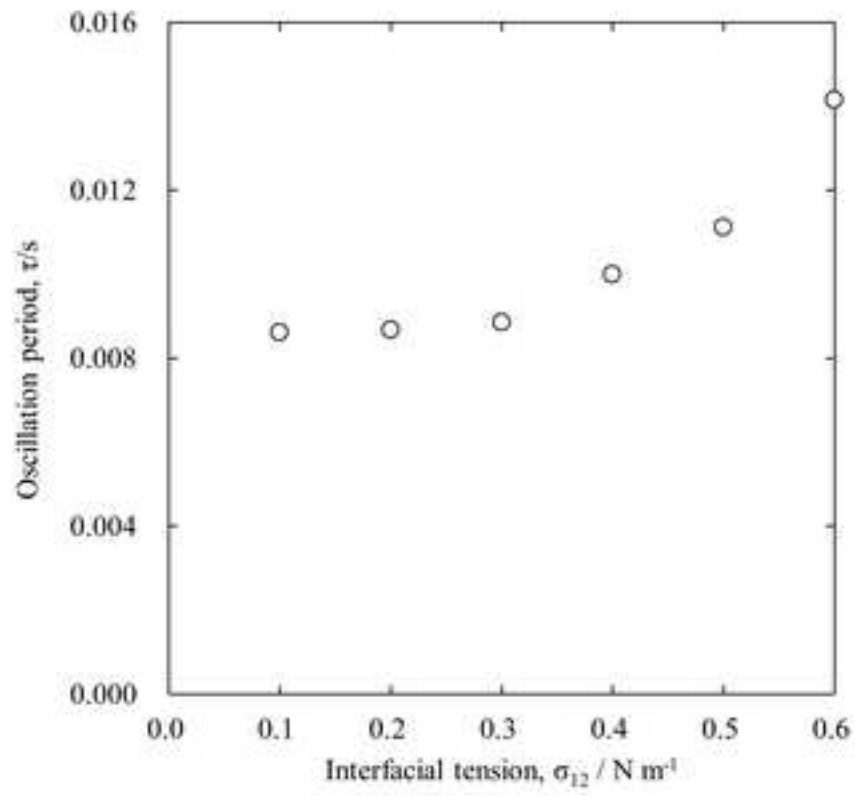


Fig.14 Oscillation periods of contacting droplet at each case.

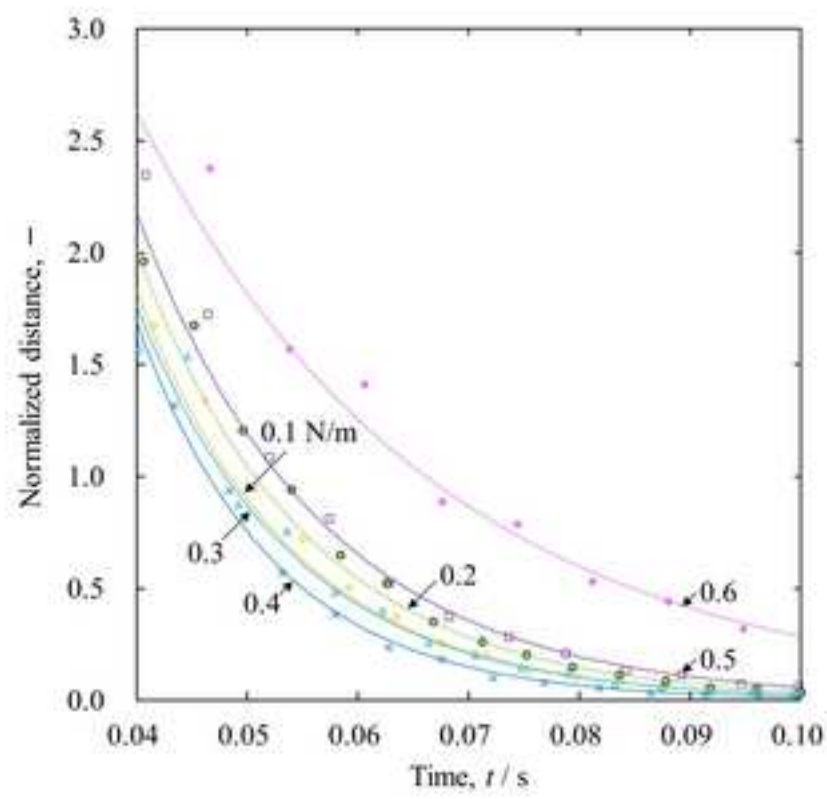


Fig.15 Influence of σ_{12} value on the damping rate of binary droplets oscillation.

Figure
[Click here to download high resolution image](#)

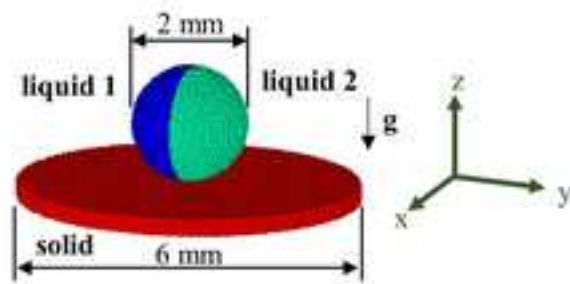


Fig.16 Initial placement for contacting two droplets on a flat plate.

Figure

[Click here to download high resolution image](#)

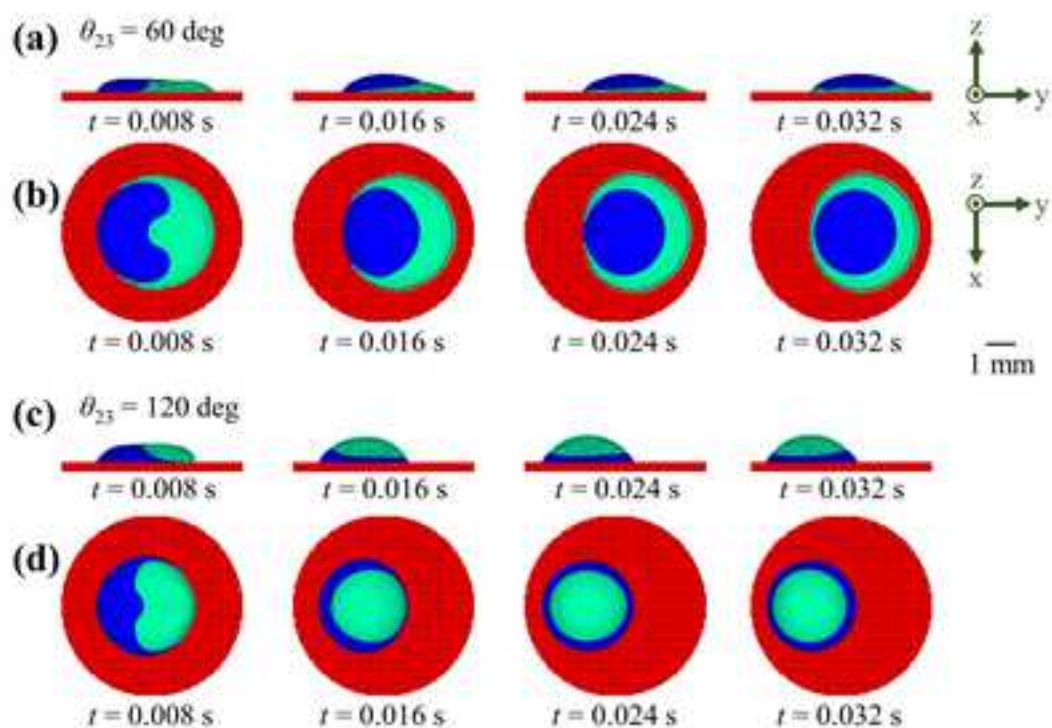


Fig.17 Time change of binary droplet morphology on a flat plate at $\theta_{23} = 60$ deg and $\theta_{23} = 120$ deg. The physical properties of droplets are identical. (a) Cross-sectional view at $\theta_{23} = 60$ deg, (b) top view at $\theta_{23} = 60$ deg, (c) cross-sectional view at $\theta_{23} = 120$ deg, (d) Top view at $\theta_{23} = 120$ deg.

Figure
[Click here to download high resolution image](#)

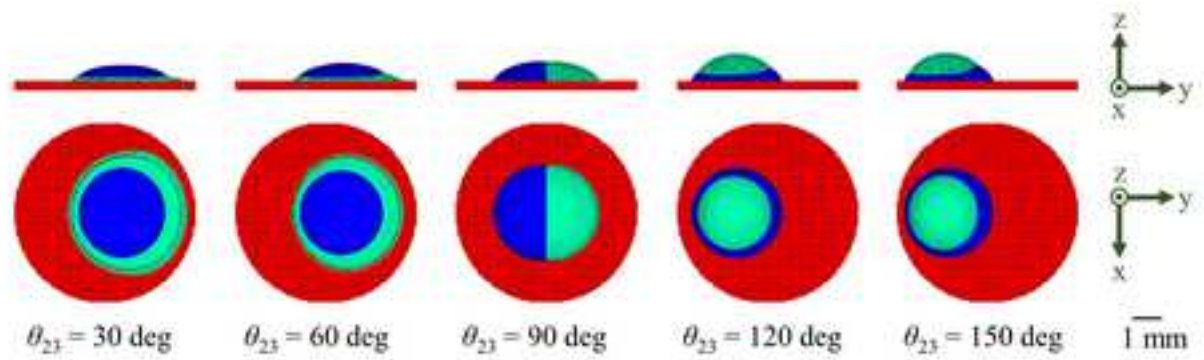


Fig.18 Snapshots of binary droplet on a flat plate at each θ_{23} condition ($t = 0.032$ s).

Figure

[Click here to download high resolution image](#)

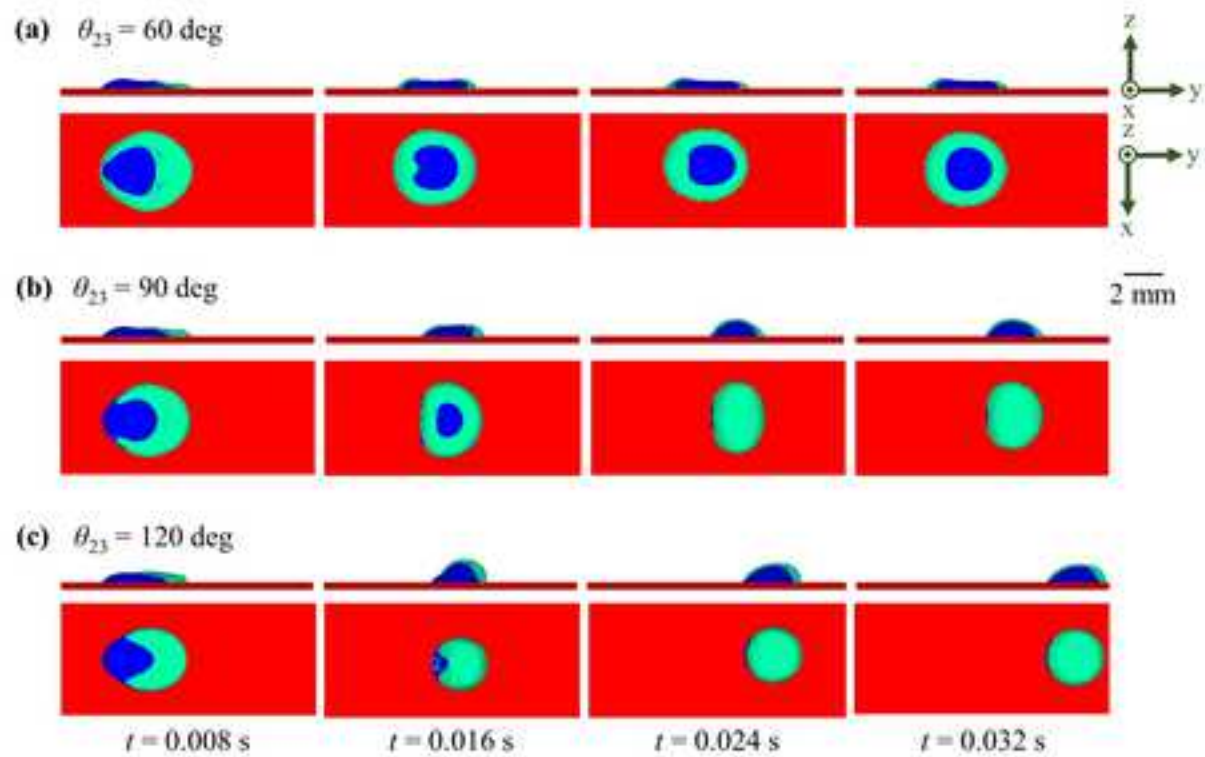


Fig. 19 Time change of binary droplet morphology on a flat disk at each θ_{23} value. The physical properties of droplets are assumed to be matte and slag. Each snapshot show the cross-sectional and top view at (a) $\theta_{23} = 60$ deg, (b) $\theta_{23} = 90$ deg, and (c) $\theta_{23} = 120$ deg.

Figure

[Click here to download high resolution image](#)

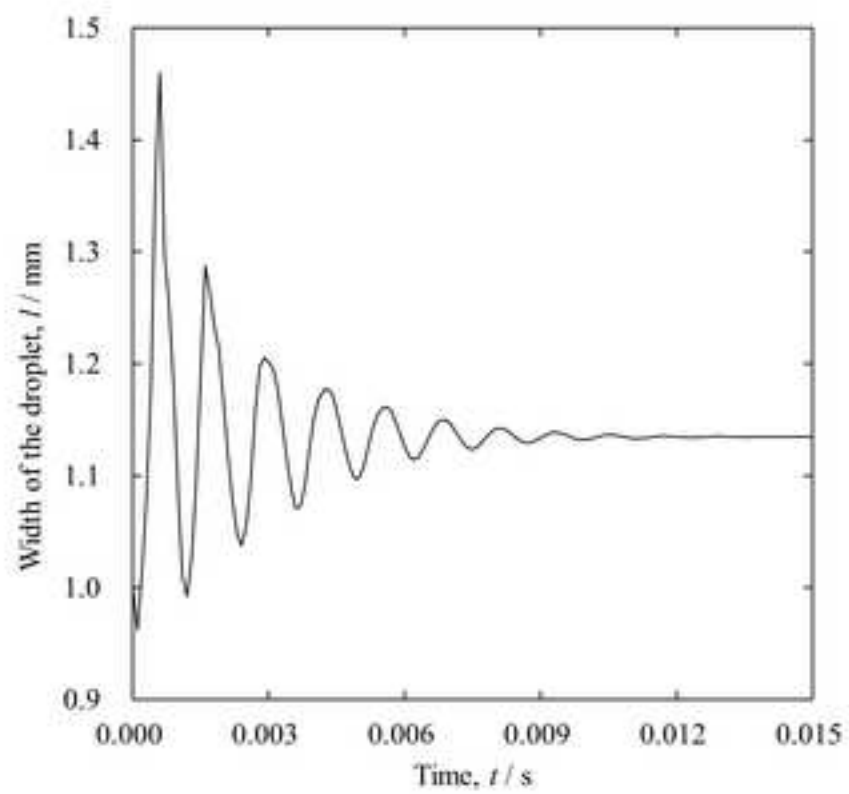


FIG. A-1. Time change of the width of the droplet when c^2 is $150 \text{ m}^2/\text{s}^2$.

Figure

[Click here to download high resolution image](#)

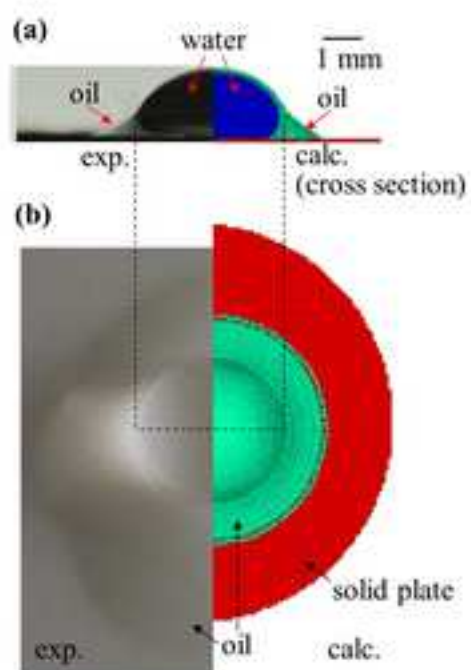


FIG. A-2. Comparison of experimental photographs and calculated shape of static water-oil contact shape on Teflon plate. (a): horizontal view, and (b): top view.

Table

[Click here to download high resolution image](#)

Table.1 The calculated values of LHS of Eq. (27) divided by σ_1 .

$\sigma_{12}, \text{N/m}$	0.1	0.2	0.3	0.4	0.5	0.6
error, %	13.9	21.5	6.0	4.8	11.8	15.3

Table

[Click here to download high resolution image](#)

Table A-1. Calculated values of oscillation period at each sound speed.

$c^2, \text{m}^2/\text{s}^2$	60	100	150	400	600
$T, 10^{-3} \text{s}$	1.16	1.17	1.24	1.38	1.46